

Aeromagnetic and spectral expressions of rare earth element deposits in Gallinas Mountains area, Central New Mexico, USA

Mo Li¹, Xiaobing Zhou¹, Christopher H. Gammons², Mohamed Khalil¹, and Marvin Speece¹

Abstract

The Gallinas Mountains, located at the junction of Lincoln and Torrance Counties, New Mexico, USA, are a series of alkaline volcanic rocks intruded into Permian sedimentary rocks. The Gallinas Mountains area hosts fluorite and copper as veins containing bastnäsite, whereas deposits of iron skarns and iron replacement are in the area as well. These deposits produce iron. In this study, the multispectral band-ratio method is used for surface mineral recognition, whereas 2D subsurface structure inversion modeling was applied to explore the depth extent of the magnetic ore distribution from aeromagnetic data. Bastnäsite has higher magnetic susceptibility (0.009 SI) than the host rocks and surrounding sedimentary rock. The bastnäsite and iron oxides (magnetite + hematite) can contribute to a positive aeromagnetic anomaly. Results indicate that (1) the positive magnetic anomaly observed at Gallinas Mountains area can be accounted for by a mixture of bastnäsite and iron oxides at a depth of approximately 400 m and a thickness of approximately 13–15 m. The surface of this area is dominated by the hydrothermal alteration associated with iron oxides over the trachyte intrusions as detected by Landsat 8 band-ratio imaging.

Introduction

Rare earth elements (REEs) have been widely used in high-technology devices and renewable energy production and as a catalyst for manufacturing industries. Given that the global demand for REE is increasing, continual exploration for potential REE deposits is important for sustainability of a hi-tech-based economy. At least 10 main REE deposits have been discovered in New Mexico; further investigation for new reserves and mineral occurrences in New Mexico's REE districts will have economic benefits in general (Long et al., 2010; McLemore, 2015).

The Gallinas Mountains district located in the northern Lincoln County and southern Torrance County of central New Mexico is a series of alkaline igneous intrusions known to have bastnäsite, a cerium-rich REE mineral, formed within fluorite-copper-sulfide deposits in the Gallinas Mountains area. Four different deposit types have been identified in the Gallinas Mountains: Cu-REE-F hydrothermal veins, epithermal REE-F veins, REE-F breccia pipes, and iron skarn deposits. All four types of deposits are related to alkaline to alkali-calcic igneous rocks (McLemore, 2010). Previous investigations of the Gallinas Mountains area have focused on geologic and tectonic formation of the mountains and

geochemical exploration. However, geophysical expressions of the REE deposits and their host rocks have not been well-investigated.

Airborne magnetism and multispectral band-ratio techniques are useful tools in detecting mineral deposits having distinct physical features. An aeromagnetic anomaly is caused by lateral variations in the magnetic susceptibility of the earth's materials that can be considered as a vector sum (total magnetization) of induced and remnant magnetization (Blakely, 1995). Igneous intrusions often cause higher magnetic anomalies than country rocks. The multispectral band-ratio method can remotely and economically detect minerals with specific spectral features linked to those materials' absorption and scattering properties. In this paper, the aeromagnetic data collected over the central New Mexico area and the precision terrain-corrected products (LIT) of Landsat 8 multispectral data were processed and interpreted to characterize surface and subsurface features of the REE deposits in the Gallinas Mountains area, central New Mexico, USA. The objectives of this study are (1) to characterize the surface mineralogical features of the study site by using the multispectral band-ratioing technique of satellite images and (2) to invert subsurface structures through 2D magnetic inverse modeling.

¹Montana Technological University, Department of Geophysical Engineering, Butte, Montana 59701, USA. E-mail: mli@mtech.edu; xzhou@mtech.edu; mkhalil@mtech.edu; mspeece@mtech.edu.

²Montana Technological University, Department of Geological Engineering, Butte, Montana 59701, USA. E-mail: cgammons@mtech.edu.

Manuscript received by the Editor 3 November 2017; revised manuscript received 25 March 2018; published ahead of production 11 July 2018. This paper appears in *Interpretation*, Vol. 6, No. 4 (November 2018); p. 1–13, 10 FIGS., 2 TABLES.

<http://dx.doi.org/10.1190/INT-2017-0199.1>. © 2018 Society of Exploration Geophysicists and American Association of Petroleum Geologists. All rights reserved.

Geologic background

The mining district in the Gallinas Mountains, along the Lincoln County Porphyry Belt (LCPB), was formed by magmatic/hydrothermal processes. The LCPB is part of the North American Cordilleran (NAC) alkaline-igneous belt (Kelley and Thompson, 1964; Kelley, 1971; Allen and Foord, 1991; McLemore and Zimmerer, 2009). The NAC belt spanning Alaska, southern British Columbia, eastern New Mexico, Texas, and Mexico contains numerous alkaline-related mineral deposits, such as gold, silver, fluorite, and REE (Lindgren, 1933; Van Alstine, 1976; Woolley, 1987; Mutschler et al., 1991; Clark, 1999). Important mineral deposits in the part of the NAC alkaline-igneous belt that is in the LCPB of central New Mexico are associated with Tertiary alkaline to subalkaline igneous rocks (McLemore, 2001, 2011). Earlier K/Ar and $^{40}\text{Ar}/^{39}\text{Ar}$ dating suggested that the Gallinas Mountains rocks in the LCPB alkaline belt were emplaced along the north-south-trending Pederal uplift approximately 38–30 Ma ago (Allen and Foord, 1991). Later, K/Ar dating suggested that the age of the trachyte/syenite of the Gallinas Mountains is 29.9 Ma, belonging to a younger magmatic event that occurred between 30 and 28 Ma ago (Robison et al., 2017).

The Gallinas Mountains district consists of altered Proterozoic and Permian sedimentary rocks intruded by igneous rocks. The Lower Proterozoic gneisses and

granites, the oldest units, are overlain by the Permian Abo Formation that is composed of arkosic conglomerate, arkose, and siltstone/shale. The Permian Yeso Formation, consisting of sandstone, siltstone, shale, limestone, and dolomite, lies between the Abo Formation and sandstones of the Glorieta Formation (Perhac, 1970; Schreiner, 1993). In the middle Tertiary, a set of shallow, porphyritic intrusions (mainly trachyte and rhyolite) was emplaced as laccoliths, which caused doming, faulting, and fracturing of the Lower Permian sedimentary rocks (Perhac, 1970; Schreiner, 1993; McLemore, 2011). The principal deposits in the New Mexico districts have been classified into four types of Great Plains Margin (GPM) deposits: GPM-iron skarn deposits, GPM-breccia pipe deposits, REE-F hydrothermal vein deposits, and Cu-REE-F hydrothermal vein deposits (North and McLemore, 1986, 1988; McLemore and Phillips, 1991; McLemore, 2010). A geologic map including locations of mines and prospects in the Gallinas Mountains area is shown in Figure 1.

The REE-F and Cu-REE-F hydrothermal veins in the Gallinas mining district were mined for fluorite in the 1950s. The cerium-rich mineral bastnäsite ($\text{Ce, La}\text{CO}_3\text{F}$) was later identified in the fluorite and copper sulfide ore during recovery of fluorite. The fluorite-copper-bastnäsite deposits in the Gallinas mining district are mostly hosted in siltstones and sandstones of the Permian Yeso Formation and in the porphyritic trachyte (Perhac, 1970; McLemore, 2010). There are several vein and breccia deposits found in the trachyte. The fluorite-copper-bastnäsite deposits are interpreted as being epithermal, having formed at relatively low temperature and shallow depth (Schreiner, 1993; McLemore, 2010). The fluorite deposits formed along the fault breccias as hydrothermal veins and mineral-rich masses filling fissures and fractures. In F-REE and Cu-F-REE breccia deposits, fluorite is the dominant mineral that is composed of up to 60% of the rock (Soulé, 1946); other abundant and associated minerals include barite, quartz, galena, and bastnäsite (Griswold, 1959; Perhac, 1970). In 1990–1991, the U.S. Bureau of Mines calculated an inferred resource of 537,000 short tons with a grade of 2.95% in REE in the Gallinas Mountains (Schreiner, 1993). The main minerals in the study area are listed in Table 1. Even though previous geologic data indicate that the REE-bearing deposits of fluorite fault breccia exposed at the surface of the study site are of low grade and lack sufficient tonnage to support mining operations, information from the drill core at the Buckhorn deposit (the east edge of the study area)

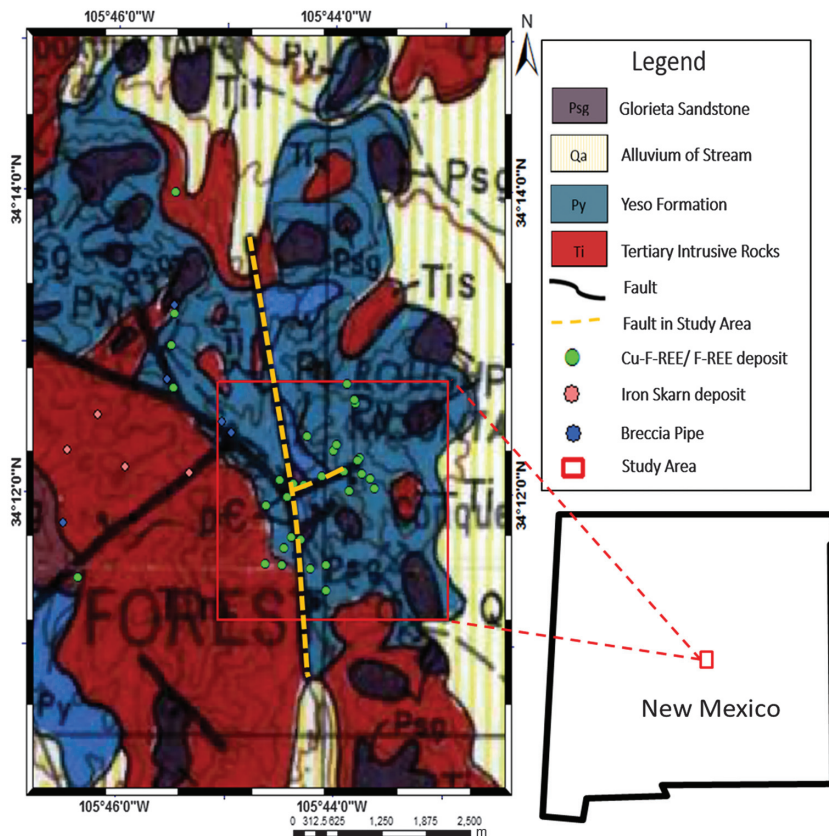


Figure 1. Geology map with the distribution of mines and prospects in the Gallinas Mountains depositional area (after Kelley, 1971; Schreiner, 1993). Iron skarn deposits are located to the west of the study site.

showed that the REE minerals can also be found at a depth greater than 135.6 m (Schreiner, 1993). In addition, data from other F-REE and Cu-F-REE mines and prospects in the study site show that REE minerals, especially bastnäsite, were found as tabular breccia zones in fluorite deposits, and the depth of the currently known deposits ranges from several tens of meters to several hundred meters.

Along with the F-REE deposits, iron skarn has been found and mined during the past few decades in the Gallinas Mountains (Figure 1). The formation of iron skarn is one stage of the hydrothermal mineralization prior to the formation of the F-REE vein deposits. The deposits show mild hydrothermal alteration and weathering of clay and iron oxides (Vance, 2013). Hypogene oxidation converted pyrite to hematite, goethite, and limonite pseudomorphs in the iron deposits. Some of the iron mines had produced a large amount of iron (mostly hematite and magnetite) before 1943. However, trenching and sampling by the New Mexico Bureau of Mines (NMBM) in 1943 showed that no additional ore can be produced from the mines. Previous studies on Gallinas Mountains rock samples suggested that fenite alteration related to carbonatite at depth may have occurred and carbonatites might be associated with hydrothermal F-REE veins buried under the trachyte intrusion, although no carbonatites have been found yet (Schreiner, 1993; McLemore, 2010; Vance, 2013).

Data

Aeromagnetic data

Aeromagnetic data are collected based on the measurement of earth's magnetic field anomalies that result from induced magnetization (dependent on the external field) and the remnant magnetism field (independent of the external field) (Hinze et al., 2013). The U.S. Geological Survey (USGS) started airborne magnetic survey in 1945 and has collected aeromagnetic data for most of the U.S., including offshore areas on both coasts. These original aeromagnetic survey data sets were collected from various flight heights and line spacing and were archived. These valuable data were compiled, standardized, and made available to the public by the USGS and National Geophysical Data Center (NGDC) in 2002 (USGS and NGDC, 2002). The aeromagnetic data set (3096C) used for this study was collected on 1 May 1976 and downloaded from the New Mexico Digital Aeromagnetic Projects (USGS and NGDC, 2002). This data set covers the southern part of the Central New Mexico area including the Gallinas Mountains (Kucks et al., 2001). The airborne magnetometer was accurate to approximately 1 nT (nanoTesla). The aeromagnetic data set was collected along 20 east–west flight lines with

1.6 km line spacing at a flight altitude of 2.6 km above sea level (Kucks et al., 2001). The aeromagnetic data were “recorded at unknown intervals” (USGS and NGDC, 2002), but after careful examination of the data, we found that the space interval between neighboring data points along each flight line varied between 64.4 and 111.4 m.

Digital elevation model

Digital elevation model (DEM) data were collected by the advanced spaceborne thermal emission and reflection radiometer (ASTER), which is an imaging instrument onboard the National Aeronautic and Space Administration (NASA) spacecraft *Terra* launched in 1999 (Yamaguchi et al., 1998). The ASTER Global DEM version 2 (GDEM2) data were released to the public by NASA and the Ministry of Economy, Trade, and Industry of Japan in October 2011 (ASTER GDEM Validation Team, 2011; Abrams et al., 2015). The ASTER instrument produces multispectral images with spatial resolution ranging from 15 to 90 m, and the GDEM2 produces DEMs having a horizontal resolution on the order of 75 m and an overall vertical accuracy of approximately 17 m. An ASTER Global DEM version 2 image ASTGTM2_N35W106 covering the Gallinas Mountains was acquired from the EarthExplorer of the USGS.

Landsat 8 image

The operational land imager (OLI) is one of the sensors onboard the Landsat 8 satellite that was launched in February 2013 (Knight and Kvaran, 2014). It has nine spectral bands, which include seven visible/near-infrared (VNIR) and two short-wave infrared (SWIR) bands. Most bands have a spatial resolution of 30 m except for the panchromatic band, which has a spatial resolution of 15 m. Spectral bands and other detailed characteristics of the OLI instrument are presented in Table 2. A terrain-corrected product (level 1 T), cloud-free Landsat-8 OLI/TIRS image (WRS2 path 33, row 36)

Table 1. Typical minerals found in the study area.

Deposit type	Mineral	Chemical formula
F-REE deposits and Cu-F-REE deposits	Quartz	SiO ₂
	Fluorite	CaF ₂
	Barite	BaSO ₄
	Calcite	CaCO ₃
	Pyrite	FeS ₂
	Bastnäsite	[Ce, La, (CO ₃)]F
	Agardite	(Ce, Ca, La)Cu ₆ (AsO ₄) ₃ (OH) ₆ ·3H ₂ O
	Parisite	Ca(Nd, Ce, La) ₂ (CO ₃) ₃ F ₂
	Xenotime	(Yb, Y, Er)PO ₄
	Monazite	(Sm, Gd, Ce, Th, Ca)(PO ₄)
	Hematite (trace)	Fe ₂ O ₃
Magnetite (trace)	Fe ₃ O ₄	

covering the Gallinas Mountains area was downloaded from the USGS (<https://earthexplorer.usgs.gov/>). The OLI/TIRS image LC80330362016294LGN00 used for this study was acquired on 20 October 2016.

METHODS

Aeromagnetic inversion method

The aeromagnetic inversion method used in this study uses the total field magnetic anomaly. The aeromagnetic measurement includes the vector sum of (1) the induced magnetic field caused by the earth's magnetic field and a rock's magnetic susceptibility and (2) the remnant magnetic field that is related to the geologic history of a rock's formation. The earth's magnetic field at the time of data collection can be calculated by the International Geomagnetic Reference Field (IGRF). IGRF is a global magnetic model that provides the earth's main magnetic field and its secular variation (Thébault et al., 2015). Remnant magnetization is usually not oriented in the

same direction as the ambient geomagnetic field and its magnitude (except for thermoremanent magnetization) is usually much smaller than the induced magnetization. The total aeromagnetic field anomalies include the induced and remnant magnetic fields, reflecting variations in the amount and type of subsurface magnetic minerals, and are thus important for geophysical prospecting of mineral resources. After subtracting the earth's magnetic field calculated using the IGRF model from the measured aeromagnetic total-field intensity, a reduction-to-the-pole (RTP) transformation was applied to the residual magnetic data to produce an RTP magnetic anomaly. RTP is a magnetic data processing procedure to remove displacements of the observed magnetic data caused by the inclination of the earth's magnetic field. The RTP magnetic anomaly was then gridded with a cell size of 200 m using the minimum curvature gridding method (O'Connell et al., 2005) and displayed as a pseudo color map in Figure 2. The selection of 200 m as the cell size for the gridded data is a compromise between the flight line spacing of 1.6 km and data point intervals of 64.4–111.4 m.

Table 2. Specification of the Landsat 8 OLI bands.

	Spectral band	Resolution (m)	Spectral range (μm)
VNIR	Band 1 — Coastal/aerosol	30	0.433–0.453
	Band 2 — Blue		0.450–0.515
	Band 3 — Green		0.525–0.600
	Band 4 — Red		0.630–0.680
	Band 5 — NIR		0.845–0.885
SWIR	Band 6 — SWIR-1	15	1.560–1.660
	Band 7 — SWIR-2		2.100–2.300
VNIR	Band 8 — Panchromatic	30	0.500–0.680
	Band 9 — Cirrus		1.360–1.390

Multispectral band ratio

Spaceborne remote-sensing techniques have been extensively used to explore natural resources on the earth's surface. Each mineral or rock has its own unique spectral signature due to specific scattering and absorption that is often used to identify a target mineral remotely. In this study, because hydrothermal alteration and iron oxide were reported to occur in the Gallinas Mountains mining district (Perhac, 1970; Schreiner, 1993; McLemore, 2010), the remote-sensing technique band ratioing and color composite imaging can help to enhance spectral contrast and to map the surface distribution of iron minerals (Rawashdeh et al., 2006; Madani, 2009; Dehnavi et al., 2010).

Iron oxides and oxide hydroxides of iron are among the most common minerals in nature. Common iron oxide minerals such as hematite (Fe_2O_3), goethite ($\alpha\text{-FeO}(\text{OH})$), magnetite (Fe_3O_4), and jarosite ($\text{KFe}_3(\text{SO}_4)_2(\text{OH})_6$) present in exposed altered rocks can produce unique spectral features within multispectral or hyperspectral satellite images. Spectral information can be used to remotely locate hydrothermally altered zones because these zones are mineralogically associated with valuable mineral deposits. Spectral features of hydrothermally altered rocks and minerals in the visible and near-infrared spectrum

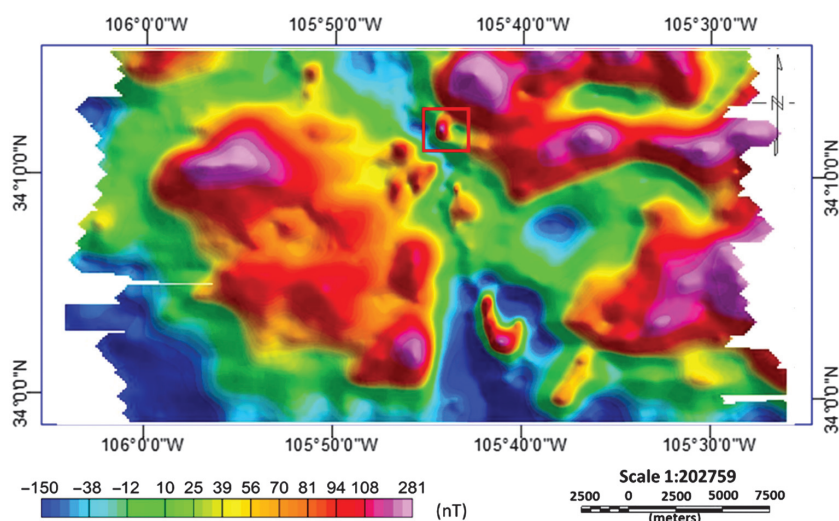


Figure 2. The spatial distribution of the RTP magnetic field of the aeromagnetic data set 3096C from USGS published in 2001. The red box shows the study site where bastnäsite, a cerium-rich REE mineral, is known to exist.

(0.35–1.0 μm) are caused by iron cations through electronic processes of crystal effects and charge-transfer absorptions (Singer, 1981), whereas features within the spectrum longer than 1.0 μm but less than 2.5 μm are caused by the vibrational transitions of hydroxyl-bearing minerals (Hunt and Ashley, 1979).

Previous studies (e.g., Hunt et al., 1971; Hunt and Ashley, 1979; Singer, 1981; Morris et al., 1985; Drury, 1993; Gupta, 2013) have observed that ferric iron oxides display distinguishable absorption features in the spectral intervals of 0.48–0.55, 0.63–0.71, and 0.85–1.00 μm . Ferrous oxides absorb light mainly at 0.45–0.55, 1.00, and 2.00–4.80 μm , whereas hydrothermal clays exhibit notable absorption features at approximately 1.90, 2.35, and 2.50 μm (Elsayed Zeinelabdein and Albiely, 2008). Band ratioing is a straightforward but powerful technique that has been widely used in mapping alteration zones and their associated minerals such as iron oxides (Segal, 1983; Sabins, 1999; Dehnavi et al., 2010; Shalaby et al., 2010). Band ratioing can enhance the contrasts between spectral reflectance curves and diminish the effect of topography and albedo (Sabins, 1999; Howari et al., 2007).

Results

Band ratioing

Previous studies showed that ores of high iron content show strong absorption in the near-infrared (approximately 0.88 μm) and far-infrared (1.71 μm) bands corresponding, respectively, to bands 5 and 6 of the OLI instrument of Landsat 8 (Guerrak, 1988; Clénet et al., 2010; Knight and Kvaran, 2014; Bersi et al., 2016). By applying the spectral features of iron oxides, which typically show high reflectance in OLI bands 4 and 6 and absorptions in bands 2 and 5, the OLI band ratios 4/2 and 6/5 were selected to highlight iron minerals in the study area (Sabins, 1999; Elsayed Zeinelabdein and Albiely, 2008; Knepper, 2010; Ducart et al., 2016). The band ratio 4/2 is useful for detecting ferric (Fe^{3+}) iron oxides such as hematite and goethite because they often show red to yellow colors in a true-color image and are absorbed in the ultraviolet and blue spectral regions (Knepper, 1989, 2010; Rockwell, 1989). Thus, the band ratio 4/2 commonly enhances the reddish color from ferric iron minerals (Sabins, 1999; Dehnavi et al., 2010; Knepper, 2010; Shalaby et al., 2010) even if they are not present in high concentration. Ferric iron minerals occur as coatings or are disseminated on the surface of hydrothermally altered rocks. Sedimentary rocks and related low-grade mafic regolith can be identified with this ratio (Dehnavi et al., 2010; Rockwell, 2013). As a result, large pixel values in the study area (the red rectangle in Figure 3) may represent rocks and soils associated with ferric iron oxides. The brightest zones in the study area are located at the central and middle left areas; a few bright spots were also observed at the bottom and top left areas. These observations may indicate the presence of soils or rocks containing ferric oxides on the surface.

OLI band 5 coincides with the absorption features of ferrous and ferric iron minerals, whereas band 6 covers the high-reflection peak for ferrous iron oxides, ferruginous saprolite, clays, hydrothermally altered rocks, and most other soils (Podwysocki et al., 1985; Wilford and Creasey, 2002). Another band ratio used in this study is OLI band ratio 6/5. This index is proposed to detect crystal-field absorption features from possible ferrous (Fe^{2+}) minerals and the ferric-ferrous iron oxide, magnetite (Kaufmann, 1988; Wilford and Creasey, 2002; Rajendran et al., 2007; Dogan, 2008, 2009; Elsayed Zeinelabdein and Albiely, 2008; Ducart et al., 2016). This index highlights ferrous iron related rocks (Figure 4). The brightness zones indicate that ferrous iron oxides mostly appear at the central and mid-left areas with a few zones in the top-left and bottom areas.

Based on the two band-ratio results above, among OLI band ratios 4/2 and 6/5, we selected ratios 4/6 and 6/7 for further iron mineral/hydrothermally altered rock detection. OLI band ratio 6/7 is a hydrothermal index. Similar to Landsat 7 ETM+ band ratio 3/5, OLI band ratio 4/6 can enhance bare rock, barren lands, ice, and snow (Sabins, 1999; Pellikka and Rees, 2009); this ratio would help to eliminate other factors from iron oxide. A false color composite image using a combination of OLI band ratios of 4/6, 4/2, and 6/7 in red, green, and blue, respectively, has been created to detect alteration zones featured by barren lands, hydroxyl-bearing minerals, and hydrothermal clays (Sabins, 1999; Elsayed Zeinelabdein and Albiely, 2008; Pellikka and Rees, 2009; Knepper, 2010; Ducart et al., 2016). A high ratio value of one color will display the pixel in a primary color of red, green, or blue; high ratio values of two colors will display the pixel as a combination of the two colors proportional to their values. High band-ratio 4/6 values

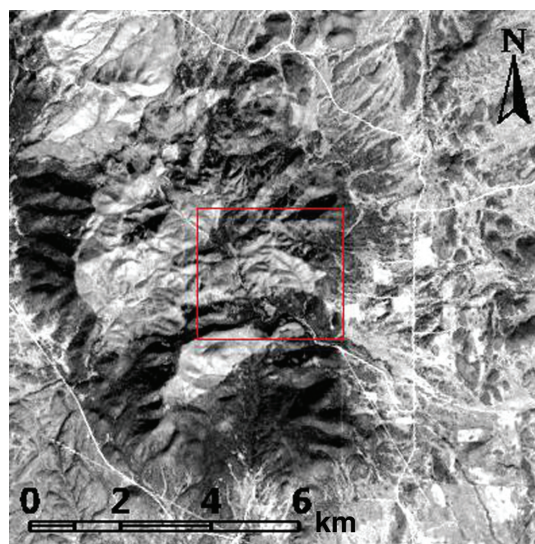


Figure 3. OLI band ratio 4/2 image covering the Gallinas Mountains area, where bright zones represent the possible presence of ferric iron oxides. The solid-line box represents the study site.

(red) give a high presence of bare rocks; large band-ratio 4/2 values (green) represent a large component of ferric oxide-associated soils; high band-ratio 6/7 values (blue) represent the presence of hydrothermal clays because band 6 covers the reflectance peak of hydrothermal clays whereas band 7 contains a reflectance trough for clays. If 4/6 and 4/2 ratio values become similarly high in the same pixel, the color of the pixel will be yellow, whereas if ratios of 4/6 and 6/7 display the same value in one pixel, the color of the pixel will be pink. As shown in Figure 5, the green zones and surrounding purple-blue zones mainly occur at the center of the study area marked by the red rectangular box, indicating the presence of hydrothermal altered clays containing disseminated iron oxides.

Distribution of aeromagnetic field intensity

The aeromagnetic total-field intensity in the central New Mexico area ranges from 52133.4 to 52347.4 nT. After removing the earth's magnetic field and the RTP transformation, an actual magnetic anomaly map is displayed in Figure 2. By draping the aeromagnetic anomaly field map onto the DEM data (left panel of Figure 6), the center of the study site shows a high positive total-field anomaly (pink). The magnetic field intensity decreases gently from the center to the margins. The anomaly is located on a northwest–southeast fault and at the end of a southwest–northeast strike fault, both of which can be observed by the dashed yellow lines in Figure 1 and the left panel of Figure 6. The two profiles shown in Figure 6 are for the segments of positive magnetic anomalies only because the 2D nonlinear inversion in the following section can be performed only for the magnetic source of positive magnetic susceptibility contrast.

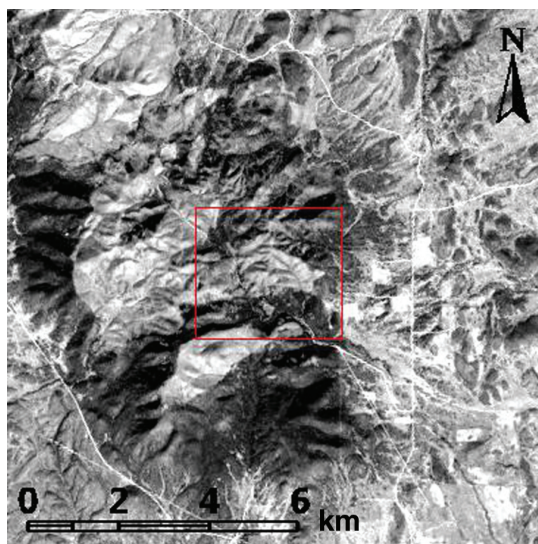


Figure 4. OLI band ratio 6/5 image covering the Gallinas Mountains area where bright zones represent the possible presence of ferrous iron oxides. The solid-line box represents the study site.

Magnetic 2D modeling

Magnetic 2D modeling is helpful in offering insights into subsurface geologic structure and magnetic mineral distribution. Aeromagnetic data of two perpendicular profiles through the study site have been used for magnetic modeling (right panel of Figure 6). Global DEM V.2 (GDEM2) data from ASTER and aeromagnetic anomaly data along the selected profiles of positive magnetic anomalies were input into GM-SYS for 2D modeling (Northwest Geophysical Associates, 2004). The physical property of rock layers needed for the 2D profile modeling is magnetic susceptibility contrast. Although many rock types in the study area have magnetic susceptibility (Griswold, 1959; Perhac, 1970; McLemore and Phillips, 1991; McLemore, 2010), two rock units are the most likely candidates to cause the local aeromagnetic highs: (1) the REE mineral bastnäsite and (2) iron oxides including magnetite and hematite. Country rocks and REE host rocks with magnetic susceptibilities less than 0.001SI will not significantly contribute to the observed magnetic field anomaly. The spectral ratio analysis and previous geology studies found no significant iron ores at shallow depths in the study area (Perhac, 1970; Schreiner, 1993). The presence of the iron oxides associated with the hydrothermal alteration at the surface of the study site and the colocated aeromagnetic positive anomaly indicate that unexploited iron oxides, hematite, and magnetite probably exist at depths during the formation of hydrothermal deposits. Therefore, we can reasonably assume that an iron oxide unit is a mixture of magnetite and other iron oxides. The average magnetic susceptibility of hematite and magnetite as a mixture is estimated from the magnetic susceptibility index (Rosenblum and Brownfield, 2000; Feral, 2010) as

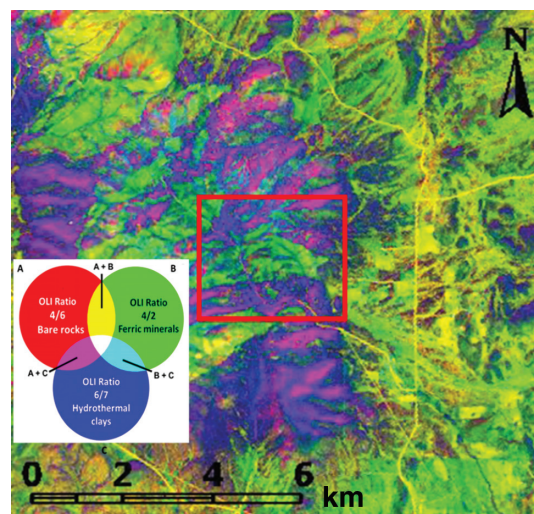


Figure 5. The false color composite image of OLI band ratios 4/6, 4/2, and 6/7 as RGB, respectively. The inset at the lower-left corner is the color addition corresponding to the mixing of barren soil (band ratio 4/6, red) and hydrothermal clays (band ratio 6/7, blue). The red box shows the study area. The green to blueish green zones at the center of the study area represent the presence of iron oxides and the associated hydrothermal clays.

0.2 SI and that of bastnäsité is taken to be 0.009 SI. The mean magnetic susceptibilities are used for each geologic unit. The boundaries of geologic units were adjusted to fit the modeled magnetic curve (solid gray lines, Figures 7 and 8) to the observed total-field aeromagnetic anomaly curve (dashed black lines, Figures 7 and 8). The depth of mineralization was assigned to be approximately 400 m below the surface as suggested by the previous geology studies and data from mines and prospects (Perhac, 1970; Schreiner, 1993; Long et al., 2010; McLemore, 2010). As previous data from mines and prospects around the study site reported, the bastnäsité formed in fluorite deposits or breccia zones appears to be tabular and the hydrothermally altered iron oxides have been found in the study site but the amount is unknown. Therefore, even though bastnäsité in fault breccia deposits could be disseminated, all bastnäsité deposits are observed at the same average depth and the large amount of brecciated veins is observed as a tabular zone in a cross-sectional view. Therefore, the target mineral bastnäsité and/or iron oxides are simplified as pure layers buried below the surface.

Figures 7 and 8 show the modeled subsurface mineralogical zones along the profiles A–A' and B–B', respectively. The four panels of Figures 7 and 8 show four subsurface mineralogical models along a west–east profile A–A' (see Figure 6). Target minerals of bastnäsité and/or iron oxides are modeled as pure layer(s) surrounded by REE host rocks. In Figures 7 and 8, bastnäsité and iron oxides are presented as dark red and yellow, respectively, the background REE bearing rocks as pink, and sandstone from Yeso Formation and granite with granitic gneiss as dark green. 15 m/2 m in Figure 7 means the equivalent average thickness of bastnäsité and iron oxide is 15 m and 2 m, respectively. The panels of Figures 9 and 10 show the corresponding subsurface mineralogical models along a northwest-to-southeast profile B–B' (Figure 6). The first model assumes that the aeromagnetic anomaly high is caused only by bastnäsité (dark red in the lower-left panel of Figure 7). A bastnäsité layer approximately 80 m thick on average produces the observed magnetic anomaly profile, with root-mean-square (rms) errors between the

observed data and the modeled response of 1.72% and 1.47% for profiles A–A' and B–B' in Figures 7 and 9, respectively. The thin red line in the top panels of Figures 7–10 shows the difference between the modeled and observed magnetic anomalies. The second mineralogical model assumes that the magnetic field

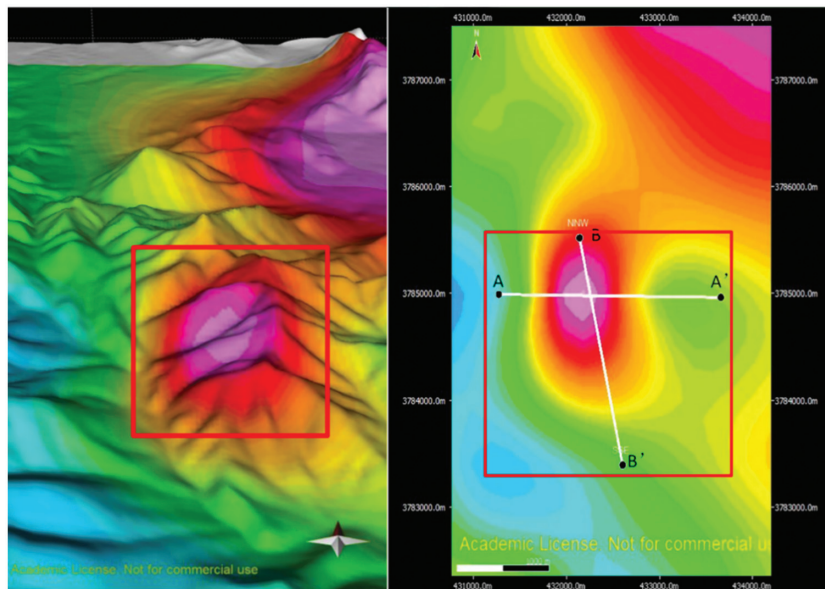


Figure 6. Left panel: the distribution of the magnetic anomaly draped over the DEM data of which the vertical elevation was exaggerated by a factor of two. Right panel: two profiles (A–A' and B–B') for 2D magnetic modeling are located over the positive magnetic anomaly.

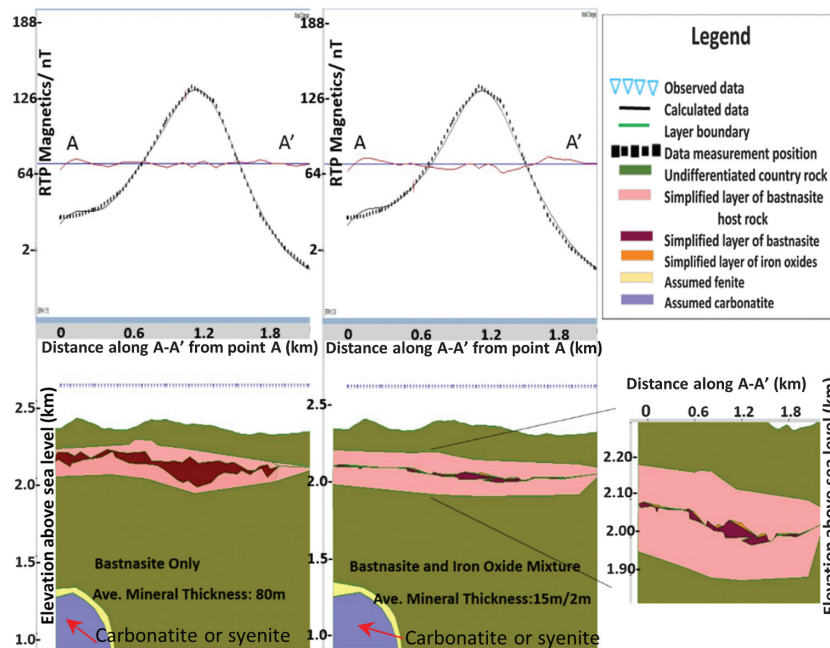


Figure 7. The 2D modeled subsurface geology along the profile A–A' assuming magnetic anomalies were caused by (1) bastnäsité only (left panel) and (2) bastnäsité and iron oxide mixture (hematite and magnetite) (right panel). The dome-shaped gray body at the lower-left corner of each panel indicates carbonatite or syenite (concealed) (McLemore, 2010).

is caused by a mixture of bastnäsité and iron oxides (hematite and magnetite). In such a case, the average thickness of iron oxides is 2 m, and the average thickness of bastnäsité is approximately 13–15 m. Such a model fits the observed magnetic anomaly profiles (A–A' and B–B') with rms errors of 1.32% and 3.12%,

respectively. The third model (lower-left panels of Figures 8 and 10) assumes that the observed magnetic anomaly high is just caused by iron oxides. In this case, the thickness of the iron oxide layer is approximately 8 m on average and the rms errors are 1.62% and 2.79% for profiles A–A' and B–B', respectively. The last

model assumes that the observed magnetic anomaly is due to magnetite with a magnetic susceptibility of 2.0 SI (Roseblum and Brownfield, 2000). In such a case, the magnetite appears as a layer (lower-right panels of Figures 8 and 10) with a thickness ranges from 0.2 to 2.0 m (0.5 m for average). The rms errors are 3.14% and 4.91%, respectively, for profiles A–A' and B–B'. The actual ores are usually not pure; therefore, the thickness of modeled pure minerals should be a mineral equivalent of the impure ore. Because the concentration of a mineral in an ore is so variable unless it is known from borehole data, using pure minerals for the interpretation of the magnetic anomaly over the Gallinas Mountains area is only from the modeling point of view. For the same equivalent thickness of a pure mineral, the actual ore thickness should be inversely proportional to the mineral concentration of the ore.

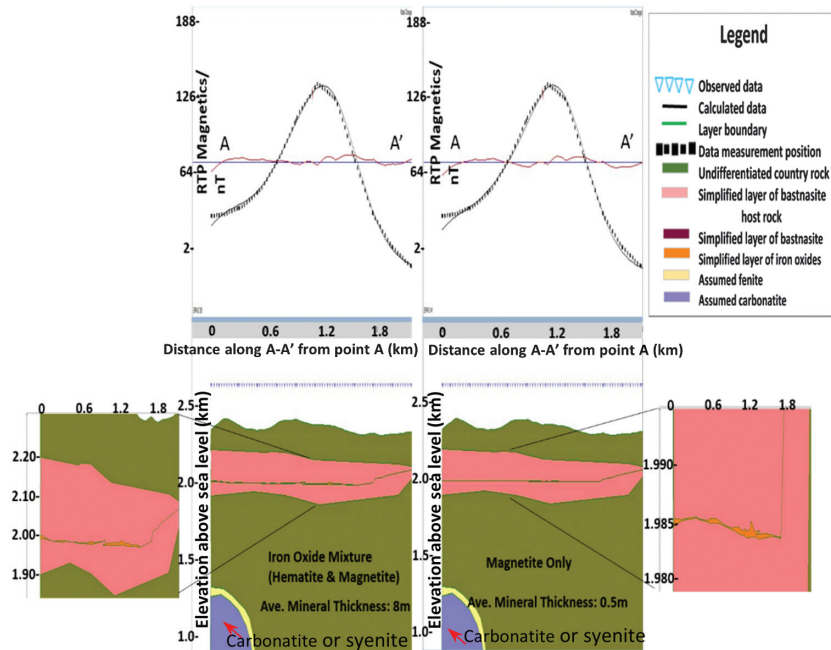


Figure 8. The 2D modeled subsurface geology along the profile A–A' assuming magnetic anomalies were caused by (3) iron oxide mixture (left panel) and (4) magnetite only (right panel). The dome-shaped gray body at the lower-left corner of each panel indicates carbonatite or syenite (concealed) (McLemore, 2010).

Discussion

Surface interpretation

The result of the Landsat 8 OLI band ratio 4/2, shown in Figure 3, indicates a possible presence of altered and weathered ferric iron oxides at the top soil in the study area. In addition, the band-ratio result also implies that iron oxides are associated with hydrothermally altered rocks. OLI band 6 corresponds to the location of high-reflection peaks of most types of rocks and soils, including hydrothermal alteration rocks, ferruginous clays, and iron oxides, whereas band 5 corresponds to the absorption band of ferric and ferrous iron-bearing minerals (Wilford and Creasey, 2002). Therefore, the high brightness values can be produced by altered rocks in association of iron oxides. Previous studies of the site show that hematite and magnetite did exist in the prospects and mines of the four types of deposits (iron skarn deposits, breccia pipe deposits, REE-F hydrothermal veins, and Cu-REE-F hydrothermal vein deposits) in the Gallinas Mountains district (Perhac, 1970; North and McLemore, 1986, 1988; McLemore and Phillips, 1991; Schreiner,

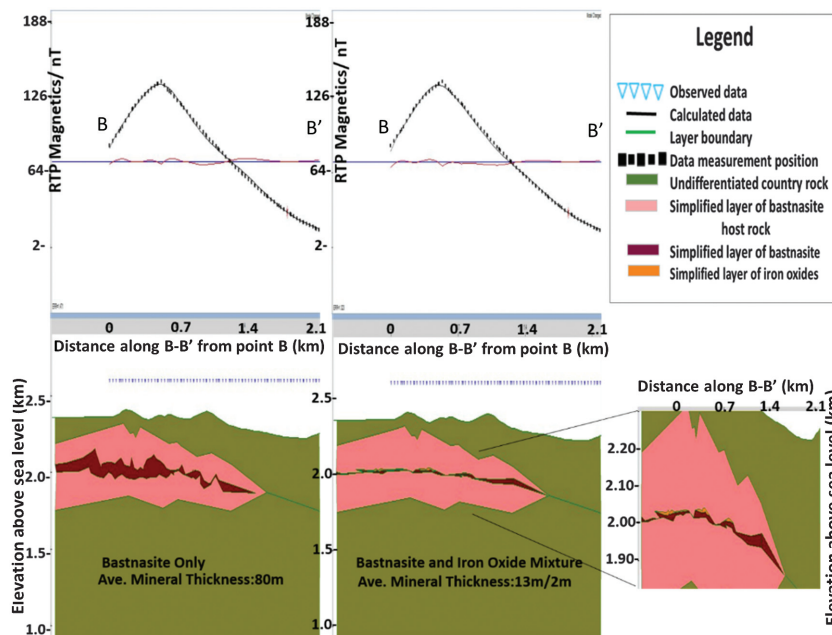


Figure 9. The 2D modeled subsurface geology along the profile B–B' assuming magnetic anomalies were caused by (1) bastnäsité only (left panel) and (2) bastnäsité and iron oxide mixture (hematite and magnetite) (right panel).

1993; McLemore, 2010). Hydrothermal alteration and the formation of iron deposits happened before the formation of hydrothermal F-REE and Cu-F-REE veins and at the end of hydrothermal activity (Schreiner, 1993; McLemore, 2010). Therefore, iron oxides could be disseminated in the top soil with low concentrations, and the high brightness values of OLI band ratios 4/2 and 6/5 may be caused by iron oxides and their associated hydrothermal clays. These results can be examined in the same ratio image as well: The bright zone to the left of the study area (Figures 3 and 4) is a series of breccias intruded into Tertiary igneous rocks. The Tertiary trachyte contains mafic minerals, which were altered to hematite and limonite ($\text{FeO}(\text{OH}) \cdot n\text{H}_2\text{O}$) and were stained by the iron-oxide-related mafic regolith. These iron oxides, although in low concentrations, have spectral features that have been detected and displayed as bright pixels in Figures 3 and 4. In the study area (the red rectangle, Figure 5), the false color RGB image displays green and bluish green at the center, blue at the top left and the bottom surrounded by pinkish purple. Figure 5 shows the color addition of an RGB composite image in which the basic color red (R) denotes OLI band ratio 4/6 showing bare rocks, green (G) denotes OLI band ratio 4/2 indicating ferric minerals, and blue (B) denotes OLI ratio 6/7 indicating clays. Thus, the composite color pink and purple represents the mixture of barren land and hydrothermal clays other than ferrous and ferric iron oxides, which coincides with Figures 3 and 4. Cyan represents a mixture of hydrothermal clays plus ferric oxides, whereas yellow represents the presence of both bare rocks in association of iron oxides. The light-gray to white zones in the ratio images (Figures 3 and 4) inside the study area coincide with green and bluish-green zones on the false-color image (Figure 5); dark-gray to black zones in the ratio images coincide with pink to purple zones in the RGB image. The RGB image matches the results of band ratios 4/2 and 6/5. The band-ratio results and false-color composite images indicate the presence of altered iron oxides and hydrothermally altered clays at the surface of the study site. These results indicate that iron oxides were deposited at the study site due to hydrothermal alteration.

Subsurface interpretation

The magnetic total-field anomaly over the Gallinas Mountains area reflects the distribution of magnetic minerals or magnetic mineral-bearing rocks. The positive magnetic anomaly observed within the study area (Figure 2) and the geologic map (Figure 1) show that iron oxides of hematite and magnetite and bastnäsite are the most likely minerals causing the observed positive magnetic anomaly. As

shown in Figures 7 and 8, we interpret the observed magnetic anomaly using four possible mineralogical models, with the content of bastnäsite varying from 100% to 0% and magnetite from 0% to 100%, respectively. The paramagnetic feature of bastnäsite results in a thick layer of bastnäsite in association of F-REE and Cu-F-REE depositional host rocks (Figures 7 and 8). The paramagnetic feature of hematite and the ferromagnetic feature of magnetite contribute to the magnetic susceptibility of iron oxides by lessening the thickness of the bastnäsite (Figures 7 and 8, case 2). We interpreted that the magnetic anomaly was caused by a layered deposit of iron oxides including hematite and magnetite (Figures 7 and 8, case 3), and magnetite only (Figures 7 and 8, case 4). The inclusion of ferric oxides and magnetite in the model decreases the amount of bastnäsite. Information from one drill core at the east edge of the study site showed that REE minerals were found relatively concentrated at a depth of 135.6 m (Schreiner, 1993). There is no known borehole within the magnetic anomaly zone to constrain the modeling, but the depth of all four types of Gallinas Mountains deposits proposed by Schreiner (1993), Richards (1995), and McLemore (2010) is within 1 km. Thus, the modeling started with the depth of the magnetic sources at 500 m in the four subsurface mineralogical models. We adjusted the top and bottom surfaces of the mineral layer iteratively to fit the calculated magnetic field to the observed field. The final results are shown in Figures 7 and 8; the final depths of the magnetic mineral layers are within 1 km, matching the previous geology studies. In addition, the simplified layered models proposed in this study fit the observed magnetic anomaly better than those models with target magnetic

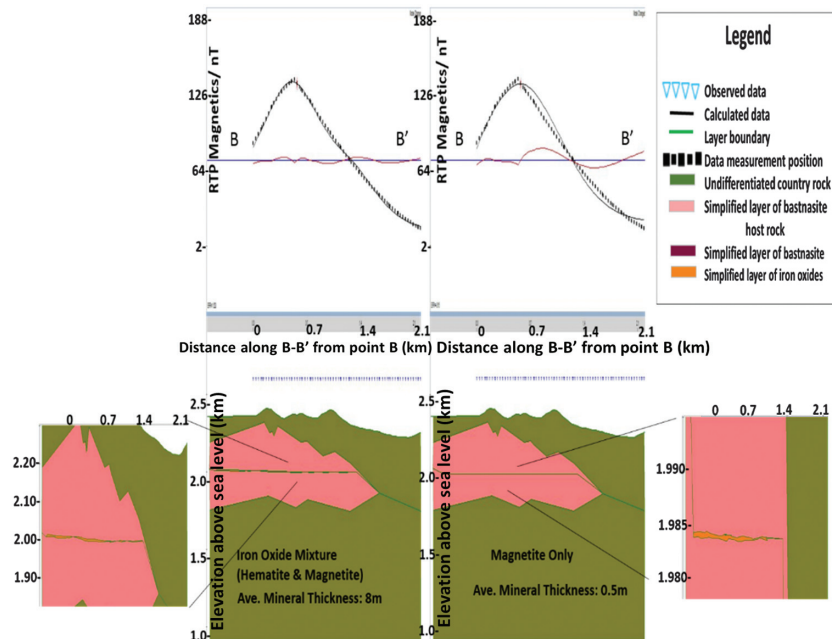


Figure 10. The 2D modeled subsurface geology along the profile *B–B'* assuming magnetic anomalies were caused by (3) iron oxide mixture (left panel) and (4) magnetite only (right panel).

minerals of layer(s) narrower in the horizontal direction, but thicker in the vertical direction that are not shown.

The mineralogical data used for this study may be not sufficient to distinguish between bastnäsite in veins at a concentration of a few percent and iron skarn/replacement deposits with Fe at 50%–70%. For this reason, we considered four subsurface mineralogical models, but the model of iron oxides and bastnäsite has a high possibility based on the present data available. Future surface mapping could help to constrain the subsurface model. In addition, the aeromagnetic data used for this study were collected in 1976 by USGS but released to the public only recently since 2002. The accuracy of the total magnetic field is approximately 1 nT. The drawbacks of this data set compared with the modern aeromagnetic data may be its lower accuracy and that no *X*-, *Y*-, and *Z*-components and gradient data were collected. With magnetic gradients available, the edges and depth of the magnetic anomalies will be more easily and accurately located.

As is shown in the surface spectral analysis using a multispectral OLI image, the presence of hydrothermal alteration and the altered iron oxides at the surface of the study area indicates that iron oxides may exist below the surface and these oxides can be a main magnetic source for the observed positive aeromagnetic anomaly. Aeromagnetic inversion along two intersecting profiles was performed with the hypothesis that the significant magnetic susceptibility contrast was due to iron oxides of magnetite and hematite and the REE mineral bastnäsite. The subsurface modeling is not unique because the exact mixing conditions of different minerals and rocks are unknown. Geologically, the magnetic anomaly may be caused by concentrated zones of bastnäsite, depositional zones of hematite and magnetite mixtures and bastnäsite, alteration zones containing a mixture of hematite and magnetite, or only deposits of magnetite. The contents of these minerals in the mineralization zones can be variable. For simplicity, we assumed the minerals for each case to be pure; otherwise, the actual thickness will increase as the concentration of the magnetic minerals for each case decreases. However, the existence of bastnäsite, hematite, and magnetite within the study site has been reported in previous geologic studies of the Gallinas Mountains depositional area (Perhac, 1970; Schreiner, 1993). The cross-sectional subsurface model having a mixture of iron oxides and bastnäsite as the magnetic source (model 2 in Figures 7 and 8) is a better match to the geologic data. The model is simplified as pure layers of magnetic minerals of bastnäsite and altered iron oxides that formed as a series of tabular and brecciated deposits distributing around the same averaged depth. This subsurface model is worth further investigation in the future by combining geophysical methods with borehole data that are not yet available. Also bastnäsite, iron oxides (hematite, magnetite), and fluorite have higher specific densities of 4.95, 5.15, 3.18 (g/cm³), respectively, than the country rocks (2.8–3.0 g/cm³) and could produce a gravity anomaly.

Additionally, bastnäsite in the breccia zones to the west of the study site is formed by filling open space caused by fentitization (Griswold, 1959; Perhac, 1970; McLemore and Phillips, 1991; Schreiner, 1993). Carbonatite is often denser, and its magnetic susceptibility is usually lower than the surrounding rocks. As a consequence, if the susceptible minerals are associated with carbonatite, then these together could be detected with gravity data. Borehole data, if available in the future, can help to constrain the depth and magnetic susceptibility values of the causative minerals for modeling, so that a more definitive and comprehensive subsurface mineralogical model can be constructed.

Conclusions

This study focused on (1) the surface mineral mapping of the southeastern Gallinas Mountains area, New Mexico, using the multispectral band-ratio images and false color images and (2) subsurface magnetic mineral location using 2D magnetic inversion of the aeromagnetic anomaly and taking into account geologic information and magnetic properties. We studied four possible models of subsurface mineralization that could give rise to magnetic anomaly highs in the area. One possibility is that bastnäsite and iron oxides exist in the southeastern Gallinas Mountains area. The study site in the southeastern Gallinas Mountain district contains a series of breccias that have been found to have mineral deposits of fluorite, copper, and bastnäsite. Hydrothermal alteration associated with iron oxides is also found over the trachyte intrusions and detected herein by band-ratio imaging. The positive aeromagnetic anomaly over the study site and the surface mineral deposits indicate the possible existence of subsurface magnetic minerals. Four subsurface mineralogical models are proposed to generate the observed magnetic anomaly. The main magnetic minerals of the four models are (1) bastnäsite, a paramagnetic REE mineral, (2) a mixture of bastnäsite and iron oxides including magnetite and hematite, (3) iron oxides of hematite and magnetite, and (4) only magnetite. Previous mineralogy and lithology studies indicate that the mineralogical model with a mixture of bastnäsite and iron oxides including hematite and magnetite to be the most likely causative magnetic source for the observed aeromagnetic anomaly. The other models are possible candidates for the observed magnetic anomaly, and borehole data are needed to eliminate the uncertainty.

Acknowledgments

This study was supported by Montana Tech and MontanaView. MontanaView is a member of the AmericaView nationwide remote-sensing consortium. We thank two anonymous reviewers and associate editor M. Khatiwada for their careful review of the manuscript and very helpful comments and suggestions that improved the quality of the manuscript.

References

- Abrams, M., H. Tsu, G. Hulley, K. Iwao, D. Pieri, T. Cudahy, and J. Kargel, 2015, The advanced spaceborne thermal emission and reflection radiometer (ASTER) after fifteen years: Review of global products: *International Journal of Applied Earth Observation and Geoinformation*, **38**, 292–301, doi: [10.1016/j.jag.2015.01.013](https://doi.org/10.1016/j.jag.2015.01.013).
- Allen, M. S., and E. E. Foord, 1991, Geological, geochemical and isotopic characteristics of the Lincoln County porphyry belt, New Mexico: Implications for regional tectonics and mineral deposits, *in* J. M. Barker, B. S. Kues, G. S. Austin, and S. G. Lucas, eds., *Geology of the Sierra Blanca, Sacramento and Capitan ranges, New Mexico*: New Mexico Geological Society, Guidebook, 42nd Field Conference, 97–113.
- ASTER GDEM Validation Team, 2011, ASTER Global Digital Elevation Model Version 2: Summary of validation results, http://www.jspacesystems.or.jp/ersdac/GDEM/ver2Validation/Summary_GDEM2_validation_report_final.pdf, accessed 8 October 2016.
- Bersi, M., H. Saibi, and M. C. Chabou, 2016, Aerogravity and remote sensing observations of an iron deposit in Gara Djebilet, southwestern Algeria: *Journal of African Earth Sciences*, **116**, 134–150, doi: [10.1016/j.jafrearsci.2016.01.004](https://doi.org/10.1016/j.jafrearsci.2016.01.004).
- Blakely, R. J., 1995, Potential theory in gravity and magnetic applications, *in* R. J. Blakely, ed., *Potential theory in gravity and magnetic applications*: Cambridge University Press.
- Clark, R. N., 1999, Spectroscopy of rocks and minerals, and principles of spectroscopy: *Manual of Remote Sensing*, **3**, 3–58.
- Clénet, H., G. Ceuleneer, P. Pinet, B. Abily, Y. Daydou, E. Harris, and C. Dantas, 2010, Thick sections of layered ultramafic cumulates in the Oman ophiolite revealed by an airborne hyperspectral survey: Petrogenesis and relationship to mantle diapirism: *Lithos*, **114**, 265–281, doi: [10.1016/j.lithos.2009.09.002](https://doi.org/10.1016/j.lithos.2009.09.002).
- Dehnavi, A. G., R. Sarikhani, and D. Nagaraju, 2010, Image processing and analysis of mapping alteration zones in environmental research, east of Kurdistan, Iran: *World Applied Sciences Journal*, **11**, 278–283.
- Dogan, H. M., 2008, Applications of remote sensing and geographic information systems to assess ferrous minerals and iron oxide of Tokat province in Turkey: *International Journal of Remote Sensing*, **29**, 221–233, doi: [10.1080/01431160701269010](https://doi.org/10.1080/01431160701269010).
- Dogan, H. M., 2009, Mineral composite assessment of Kelkit River Basin in Turkey by means of remote sensing: *Journal of Earth System Science*, **118**, 701–710, doi: [10.1007/s12040-009-0059-9](https://doi.org/10.1007/s12040-009-0059-9).
- Drury, S. A., 1993, *Image interpretation in geology*: Chapman and Hall.
- Ducart, D. F., A. M. Silva, C. L. B. Toledo, and L. M. D. Assis, 2016, Mapping iron oxides with Landsat-8/OLI and EO-1/Hyperion imagery from the Serra Norte iron deposits in the Carajás Mineral Province, Brazil: *Brazilian Journal of Geology*, **46**, 331–349, doi: [10.1590/2317-4889201620160023](https://doi.org/10.1590/2317-4889201620160023).
- Elsayed Zeinelabdein, K. A., and A. I. Albiely, 2008, Ratio image processing techniques: A prospecting tool for mineral deposits, Red Sea Hills, NE Sudan: *The International Archives of the Photogrammetry, Remote Sensing and Spatial Information Sciences*, **37**, 1295–1298.
- Feral, K., 2010, Magnetic susceptibility index for gemstones, https://www.gemstonemagnetism.com/magnetic_index.html, accessed 8 May 2017.
- Griswold, G. B., 1959, Mineral deposits of Lincoln County, New Mexico: *New Mexico Bureau of Mines and Mineral Resources, Bulletin*, 117.
- Gupta, R. P., 2013, *Remote sensing geology*: Springer Science and Business Media.
- Guerrak, S., 1988, Geology of the early Devonian oolitic iron ore of the Gara Djebilet field, Saharan Platform, Algeria: *Ore Geology Reviews*, **3**, 333–358, doi: [10.1016/0169-1368\(88\)90026-1](https://doi.org/10.1016/0169-1368(88)90026-1).
- Hinze, W. J., R. R. Von Frese, R. Von Frese, and A. H. Saad, 2013, *Gravity and magnetic exploration: Principles, practices, and applications*: Cambridge University Press.
- Howari, F. M., A. Baghdady, and P. C. Goodell, 2007, Mineralogical and geomorphological characterization of sand dunes in the eastern part of United Arab Emirates using orbital remote sensing integrated with field investigations: *Geomorphology*, **83**, 67–81, doi: [10.1016/j.geomorph.2006.06.015](https://doi.org/10.1016/j.geomorph.2006.06.015).
- Hunt, G. R., and R. P. Ashley, 1979, Spectra of altered rocks in the visible and near infrared: *Economic Geology*, **74**, 1613–1629, doi: [10.2113/gsecongeo.74.7.1613](https://doi.org/10.2113/gsecongeo.74.7.1613).
- Hunt, G. R., J. W. Salisbury, and C. J. Lenhoff, 1971, Visible and near-infrared spectra of minerals and rocks. III: Oxides and hydroxides: *Modern Geology*, **2**, 195–205.
- Kaufmann, H., 1988, Mineral exploration along the Aqaba-Levant structure by use of TM-data: Concepts, processing and results: *International Journal of Remote Sensing*, **9**, 1639–1658, doi: [10.1080/01431168808954966](https://doi.org/10.1080/01431168808954966).
- Kelley, V. C., 1971, *Geology of the Pecos country, southeastern New Mexico*: State Bureau of Mines and Mineral Resources, Memoir 24.
- Kelley, V. C., and T. B. Thompson, 1964, Tectonics and general geology of the Ruidoso-Carrizozo region, central New Mexico, *in* S. R. Ash and L. R. Davis eds., *Guidebook of Ruidoso Country (New Mexico)*: New Mexico Geological Society 15th Annual Fall Field Conference Guidebook, 110–121.
- Knepper, D. H., 1989, Mapping hydrothermal alteration with Landsat thematic mapper data, *in* K. Lee, D. H. Knepper, Jr., F. A. Kruse, R. W. Marrs, and N. M. Milton, eds., *Remote sensing in exploration geology: Golden, Colorado to Washington, D.C., June 30–July 8, 1989*: American Geophysical Union 182, 13–21.
- Knepper, D. H., 2010, Distribution of potential hydrothermally altered rocks in central Colorado derived from

- Landsat Thematic Mapper data: A geographic information system data set: U.S. Geological Survey Open-File Report 2010-1076.
- Knight, E. J., and G. Kvaran, 2014, Landsat-8 operational land imager design, characterization and performance: *Remote Sensing*, **6**, 10286–10305, doi: [10.3390/rs61110286](https://doi.org/10.3390/rs61110286).
- Kucks, R. P., P. L. Hill, and C. E. Heywood, 2001, New Mexico aeromagnetic and gravity maps and data: A web site for distribution of data: U.S. Geological Survey, Open-File Report 01–0061.
- Lindgren, W., 1933, Mineral deposits: McGraw-Hill Book Co..
- Long, K. R., B. S. Van Gosen, N. K. Foley, and D. Cordier, 2010, The principal rare earth elements deposits of the United States — A summary of domestic deposits and a global perspective: U.S. Geological Survey Scientific Investigations Report 2010–5220.
- Madani, A. A., 2009, Utilization of Landsat ETM + data for mapping gossans and iron rich zones exposed at Bahrah area, Western Arabian Shield, Saudi Arabia: *Journal of King Abdulaziz University: Earth Sciences*, **20**, 25–49.
- McLemore, V. T., 2001, Silver and gold resources in New Mexico: New Mexico Bureau of Geology and Mineral Resources, Resource Map 21.
- McLemore, V. T., 2010, Geology and mineral deposits of the Gallinas Mountains, Lincoln and Torrance Counties, New Mexico; preliminary report: New Mexico Bureau of Geology and Mineral Resources, Open-file report OF-532.
- McLemore, V. T., 2011, Geology and mineral deposits of the Gallinas Mountains REE deposit, Lincoln and Torrance Counties, NM; Preliminary report: Presented at the SME Annual Meeting, 11–139.
- McLemore, V. T., 2015, Rare earth elements (REE) deposits in New Mexico: Update: *New Mexico Geology*, **37**, 59–69.
- McLemore, V. T., and R. S. Phillips, 1991, Geology of mineralization and associated alteration in the Capitan Mountains. Lincoln County, New Mexico: New Mexico Geological Society, Guidebook 42, 291–298.
- McLemore, V. T., and M. Zimmerer, 2009, Magmatic activity and mineralization along the Capitan, Santa Rita, and Morenci lineaments in the Chupadera Mesa Area, Central New Mexico: New Mexico Geological Society, Guidebook 60, 375–386.
- Morris, R. V., H. V. Lauer, C. A. Lawson, E. K. Gibson, G. A. Nace, and C. Stewart, 1985, Spectral and other physico-chemical properties of submicron powders of hematite (α -Fe₂O₃), maghemite (γ -Fe₂O₃), magnetite (Fe₃O₄), goethite (α -FeOOH), and lepidocrocite (γ -FeOOH): *Journal of Geophysical Research: Solid Earth*, **90**, 3126–3144, doi: [10.1029/JB090iB04p03126](https://doi.org/10.1029/JB090iB04p03126).
- Mutschler, F. E., T. C. Mooney, and D. C. Johnson, 1991, Precious metal deposits related to alkaline igneous rocks: A space-time trip through the Cordillera: *Mining Engineering*, **43**, 304–309.
- North, R. M., and V. T. McLemore, 1986, Silver and gold occurrences in New Mexico; Resource Map 15; Scale 1:1,000,000; New Mexico Bureau of Mines and Mineral Resources: Socorro, 32 p.
- North, R. M., and V. T. McLemore, 1988, A classification of the precious metal deposits of New Mexico, in R. W. Schafer, J. J. Cooper, and P. G. Vikre, eds., Bulk mineable precious metal deposits of the Western United States symposium volume, proceedings, Geological Society of Nevada, 625–660.
- Northwest Geophysical Associates Inc., 2004, GM-SYS gravity/magnetic modeling software: User's guide, Version 4.9, 1–101.
- O'Connell, M. D., R. S. Smith, and M. A. Vallee, 2005, Gridding aeromagnetic data using longitudinal and transverse horizontal gradients with the minimum curvature operator: *The Leading Edge*, **24**, 142–145, doi: [10.1190/1.1876036](https://doi.org/10.1190/1.1876036).
- Perhac, R. M., 1970, Geology and mineral deposits of the Gallinas Mountains, Lincoln and Torrance counties: New Mexico State Bureau of Mines and Mineral Resources, Bulletin, **95**, 51.
- Pellikka, P., and W. G. Rees, 2009, Remote sensing of glaciers: Techniques for topographic, spatial and thematic mapping of glaciers: Taylor & Francis, 340.
- Podwysocki, M. H., M. S. Power, and O. D. Jones, 1985, Preliminary evaluation of the Landsat-4 thematic mapper data for mineral exploration: *Advances in Space Research*, **5**, 13–20, doi: [10.1016/0273-1177\(85\)90252-2](https://doi.org/10.1016/0273-1177(85)90252-2).
- Rajendran, S., A. Thirunavukkaraasu, B. Poovalinganesh, K. V. Kumar, and G. Bhaskaran, 2007, Discrimination of low-grade magnetite ores using remote sensing techniques: *Journal of the Indian Society of Remote Sensing*, **35**, 153–162, doi: [10.1007/BF02990779](https://doi.org/10.1007/BF02990779).
- Rawashdeh, S. A., B. Saleh, and M. Hamzah, 2006, The use of remote sensing technology in geological investigation and mineral detection in El Azraq-Jordan: *European Journal of Geography*, **358**, 1–21, doi: [10.4000/cybergeogeo.2856](https://doi.org/10.4000/cybergeogeo.2856).
- Richards, J. P., 1995, Alkalic-type epithermal gold deposits: A review, in J. F. H. Thompson, ed., Magmas, fluids and ore deposits: Mineralogical Association of Canada, Short Course, 367–400.
- Robison, A., W. McIntosh, and V. W. Lueth, 2017, ⁴⁰Ar/³⁹Ar geochronology of magmatism and alteration in the Gallinas Mountains with implications for rare earth mineralization: New Mexico Geological Society Spring Meeting Program, New Mexico Geology, 39, <http://nmgms.nmt.edu/meeting/abstracts/view.cfm?aid=540>, accessed 10 June 2016.
- Rockwell, B. W., 1989, Hydrothermal alteration mapping in spectral ratio feature space using TM reflectance data — Aurora mining district, Mineral County, Nevada: Proceedings of the Seventh Thematic Conference on Remote Sensing Exploration Geology, Calgary, AB, Canada, ERIM, 1189–1203.

- Rockwell, B. W., 2013, Automated mapping of mineral groups and green vegetation from Landsat Thematic Mapper imagery with an example from the San Juan Mountains, Colorado: U.S. Geological Survey Scientific Investigations Map 3252, 25 p. pamphlet, 1 map sheet, scale 1:325,000, <https://pubs.usgs.gov/sim/3252/>, accessed on 20 February 2017.
- Rosenblum, S., and I. K. Brownfield, 2000, Magnetic susceptibilities of minerals (No. 99-529): U.S. Geological Survey, Open-File Report 99-0529.
- Sabins, F. F., 1999, Remote sensing for mineral exploration: *Ore Geology Reviews*, **14**, 157–183, doi: [10.1016/S0169-1368\(99\)00007-4](https://doi.org/10.1016/S0169-1368(99)00007-4).
- Schreiner, R. A., 1993, Mineral investigation of the rare-earth-element-bearing deposits. Red Cloud mining district, Gallinas Mountains, Lincoln County, New Mexico: US Bureau of Mines, Open File Report, 93–99, https://geoinfo.nmt.edu/staff/mclemore/documents/99-93_000.pdf.
- Segal, D. B., 1983, Use of Landsat multispectral scanner data for the definition of limonitic exposures in heavily vegetated areas: *Economic Geology*, **78**, 711–722, doi: [10.2113/gsecongeo.78.4.711](https://doi.org/10.2113/gsecongeo.78.4.711).
- Shalaby, M. H., A. Z. Bishta, M. E. Roz, and M. A. El-Zalaky, 2010, Integration of geologic and remote sensing studies for the discovery of uranium mineralization in some granite plutons, Eastern Desert, Egypt: *Journal of King Abdulaziz University: Earth Sciences*, **21**, 1–25.
- Singer, R. B., 1981, Near-infrared spectral reflectance of mineral mixtures: Systematic combinations of pyroxenes, olivine, and iron oxides: *Journal of Geophysical Research: Solid Earth*, **86**, 7967–7982, doi: [10.1029/JB086iB09p07967](https://doi.org/10.1029/JB086iB09p07967).
- Soulé, J. H., 1946, Exploration of the White Eagle Fluorspar Mine, Cooks Peak mining district, Grant County, New Mexico: United States Bureau of Mines, War Minerals Report 125.
- Thébault, E., C. C. Finlay, C. D. Beggan, P. Alken, J. Aubert, O. Barrois, F. Bertrand, T. Bondar, A. Boness, L. Brocco, E. Canet, A. Chambodut, A. Chulliat, P. Coisson, F. Civet, A. Du, A. Fournier, I. Fratter, N. Gillet, B. Hamilton, M. Hamoudi, G. Hulot, T. Jager, M. Korte, W. Kuang, X. Lalanne, B. Langlais, J.-M. Leger, V. Lesur, F. J. Lowes, S. Macmillan, M. Manda, C. Manoj, S. Maus, N. Olsen, V. Petrov, V. Ridley, M. Rother, T. J. Sabaka, D. Saturnino, R. Schachtschneider, O. Siro, A. Tangborn, A. Thomson, L. Toffner-Clausen, P. Vigneron, I. Wardinski, and T. Zvereva, 2015, International geomagnetic reference field: The 12th generation: *Earth, Planets and Space*, **67**, 79, doi: [10.1186/s40623-015-0228-9](https://doi.org/10.1186/s40623-015-0228-9).
- USGS (U.S. Geological Survey) and NGDC (National Geophysical Data Center), 2002, Digital aeromagnetic datasets for the conterminous United States and Hawaii — A companion to the North American magnetic anomaly map: USGS Open-File-Report 02-361, 2002, <https://pubs.usgs.gov/of/2002/ofr-02-361/>, accessed 18 January 2016.
- Van Alstine, R. E., 1976, Continental rifts and lineaments associated with major fluorspar districts: *Economic Geology*, **71**, 977–987, doi: [10.2113/gsecongeo.71.6.977](https://doi.org/10.2113/gsecongeo.71.6.977).
- Vance, Z., 2013, Mineralogy, geochemistry and genesis of the hydrothermal REE-fluorite-AG-PB-CU ore deposits of the Gallinas Mountains, New Mexico: Doctoral dissertation, New Mexico Institute of Mining and Technology.
- Wilford, J., and J. Creasey, 2002, Landsat thematic mapper, in É. Papp, ed., *Geophysical and remote sensing methods for regolith exploration*: CRCLEME Open File Report 144, 6–12.
- Woolley, A. R., 1987, Alkaline rocks and carbonatites of the World. Part 1: North and South America: British Museum (Natural History); University of Texas Press.
- Yamaguchi, Y., A. B. Kahle, H. Tsu, T. Kawakami, and M. Pniel, 1998, Overview of advanced space borne thermal emission and reflection radiometer (ASTER): *IEEE Transactions on Geoscience and Remote Sensing*, **36**, 1062–1071, doi: [10.1109/36.700991](https://doi.org/10.1109/36.700991).

Biographies and photographs of the authors are not available.